IEEE Access
Multidisciplinary | Rapid Review | Open Access Journal

Received July 3, 2021, accepted July 14, 2021, date of publication August 13, 2021, date of current version August 24, 2021.

Digital Object Identifier 10.1109/ACCESS.2021.3104642

Topology Optimization of Rotor Bars Geometry and Arrangement for a Line-Start Permanent Magnet Synchronous Machine

JAN BARTA[1], LADISLAV KNEBL[1], GERD BRAMERDORFER[2], (Senior Member, IEEE), IVETA LOLOVA[1], SIEGFRIED SILBER[3], (Member, IEEE), AND ONDREJ VITEK[1]

[1]Department of Power Electrical and Electronic Engineering, Brno University of Technology, 61600 Brno, Czechia
[2]Institute of Electrical Drives and Power Electronics, Johannes Kepler University Linz, 4040 Linz, Austria
[3]Linz Center of Mechatronics, 4040 Linz, Austria

Corresponding author: Jan Barta (bartaj@vutbr.cz)

This research work has been carried out in the Centre for Research and Utilization of Renewable Energy (CVVOZE). Authors gratefully acknowledge financial support from the Ministry of Education, Youth and Sports under institutional support and BUT specific research programme (project No. FEKT-S-20-6379). Furthermore, this work has been supported by the COMET-K2 "Center for Symbiotic Mechatronics" of the Linz Center of Mechatronics (LCM) funded by the Austrian federal government and the federal state of Upper Austria.

ABSTRACT An optimally designed line-start permanent magnet synchronous machine may require a different squirrel-cage design than traditional induction machines. The objective of this paper is to apply topology optimization based on the normalized Gaussian network in order to find the optimal shape of the rotor bars for a line-start permanent magnet synchronous machine. This approach facilitates optimizing the shape of the bar, without the limitation of a predefined bar geometry and arrangement, as is usually considered for classic induction machine design. For this study, a previously designed four-pole line-start permanent magnet synchronous machine with a rated power of 1.5 kW is used as an initial design. To verify the accuracy of performance evaluation by utilizing finite-element methods, a prototype of this machine was built and tested. Then, verified model of line-start permanent magnet machine is used for topology optimization of its rotor cage area. The outcome of the optimization is the Pareto front, from which three optimized designs are selected. Finally, these designs are analyzed and proved to have better steady-state performance than the initial machine. The results provide new insights for the design of squirrel-cage bars for line-start permanent magnet synchronous machines.

INDEX TERMS AC machines, line-start permanent magnet machine, optimization, permanent magnet machines.

I. INTRODUCTION

Since line-start permanent magnet synchronous machines (LSPMSMs) appear to be a promising machine type for meeting high-efficiency-class demands, many authors have dealt with their design in recent years [1]. Generally speaking, a LSPMSM is a permanent magnet synchronous machine (PMSM) equipped with a squirrel-cage for asynchronous starting, similar to the one used in an induction machine. The idea behind this combination is to achieve a design with the benefits of both IM and a PMSM. As a result, the LSPMSM can provide higher efficiency for the same output power in a comparable frame size, it runs at synchronous speed, and it features higher power factor than the IM. The key concept of the improvement in efficiency is the reduction of the rotor and stator Joule losses. LSPMSMs can start directly from the grid without the need for power electronics, all while being able to achieve higher efficiency classes than classic IMs [2], [3]. Moreover, as has been demonstrated in [4], the lower losses of LSPMSMs enable a significant extension of the variable speed drive (VSD) constant power range when compared to IM VSDs.

On the other hand, a LSPMSM suffers from several problems such as limited start-up capability, cogging, noise, and vibration. This makes the design process for LSPMSMs very complex. Designers have to adjust the design of the machine to achieve acceptable performance during start-up and steady-state, and the machine should be able to synchronize with the demanded load connected to the machine shaft. The complexity of LSPMSM theory, together with

The associate editor coordinating the review of this manuscript and approving it for publication was Paolo Giangrande.

a description of synchronizing phenomena and related analytical equations, can be found in [5] and [6], and fault diagnosis for LSPMSMs has been investigated in [7]–[9].

The stator of a LSPMSM can be the same as that used in the IM counterpart. The main difference between LSPMSMs and IMs is in the rotor design. Various rotor configurations for a LSPMSM together with an idea of using the same lamination for various pole combinations are presented in [10]. The advantage of the presented solution is that motors with various numbers of poles can all be built using the same mold. Studies and comparisons of different rotor topologies for a low-power 3.7 kW LSPMSM are provided in [11] and [12]. Within those papers, topologies manufactured by applying wire cutting from commercial IM rotors are suggested, this can be an impractical approach if serial and cost effective production of LSPMSM is required. Special rotor topologies comparison of the combination of surface-mounted magnets and aluminum ring, solid rotor with interior permanent magnets and U-shaped magnets was reported in [13] for 22 kW six-pole LSPMSM. Spoke magnet configuration for building a high-efficiency LSPMSM from 600 W squirrel-cage IM was shown in [14]. Other investigated rotor designs for LSPMSM can be found in [15].

The challenges of their design is one of the reasons why LSPMSMs are often configured by making use of optimization techniques [1]. Such design approaches have been presented in many papers. Optimization of LSPMSMs utilizing the genetic algorithm together with an analysis of both steady-state and dynamic capabilities is demonstrated in [10]. The development of a three-phase 3.7 kW two-pole LSPMSM by optimization of the rotor structure using surface-response methodology is presented in [16]. Another LSPMSM design using the genetic optimization algorithm is studied in [17], and optimization based on an analytical model with incorporation of the starting capability as a constraint is demonstrated in [18]. The conducted optimization focuses only on the shape of the magnet cavity, and the magnet dimensions, but the shape of the rotor bars is not considered.

Many articles have dealt with approaches other than optimization to improve the properties of LSPMSMs. In [19], the authors studied the possibilities of starting performance improvement by changing the stator winding configurations. Further, the method based on pole changing of LSPMSM was studied in [20].

Nonetheless, the majority of previous works has dealt with LSPMSMs using the same predefined geometry for optimization based on the squirrel-cage bars adopted from classic IMs. Furthermore, no activities are reported that deal with topology optimization (TO) [21] for LSPMSM performance improvement. This is in contrast to PMSMs, where many such studies can be found, e.g. in [22], as well as for synchronous reluctance machines, e.g. [23], [24]. The major reason could be the high calculation demands that arise when the machine's ability to synchronize must be verified. To address this, the research presented here is focused on the general optimization of the rotor bar slot shape for LSPMSMs. To avoid the limitation associated with a predefined parametrized geometry, TO based on the normalized Gaussian network (NGnet) is used.

In order to speed up the TO of the LSPMSM, an appropriate approach has been developed, and it is described together with the adopted TO and NGnet in Section II. The whole study is conducted on a specific machine that has been manufactured to verify the calculated performance by finite element analysis (FEA), and this is the subject of Section III. The following Section IV is dedicated to presenting the research results and a comprehensive analysis of the rated-load, no-load, and starting performance. A brief discussion of the manufacturability of optimized designs is further given in Section V. The paper is concluded in Section VI.

II. TOPOLOGY OPTIMIZATION

TO can be used to find a novel shape for electrical machines. For example, this approach has been applied to the optimization of the rotor geometry of a PMSM through utilizing a genetic algorithm in [25], and a combination of rotor core TO with identification of current phase angle was described in [26]. TO is not limited to electrical machine design but can be implemented for a huge variety of technical problems [21].

A geometrical shape featuring two different materials can be optimized by considering two binary states, ON/OFF, and using an appropriate optimization algorithm. An example of such an approach is shown in Fig. 1(a). In this figure, the design region is divided into several cells. The material of each cell is defined by the state-of-cell variable $S(x, y)$. Although this method can find an optimal solution, the optimization is very time-consuming due to the large number of cells to which the state-of-cell variable has to be assigned. In addition, it is known that this practice can lead to non-manufacturable and complicated geometries [24].

To overcome this disadvantage, the adopted topology optimization method is based on the NGnet which is comprehensively described in [24] and [27]. This method, introduced by Sato *et al.*, facilitates obtaining smooth shapes in the resulting geometry in a shorter time than simple ON/OFF based TO.

According to [24], NGnet is defined by the weighted sum of the normalized Gaussian functions, as follows:

$$f(x, y) = \sum_{i=1}^{N} w_i b_i(x, y), \tag{1}$$

where w_i is the weighting coefficient, N is the number of the Gaussian functions, and $b_i(x, y)$ is computed from

$$b_i(x, y) = \frac{G_i(x, y)}{\sum_{j=1}^{N} G_j(x, y)}. \tag{2}$$

The resulting NGnet is used to determine the material assignment for each considered cell through the state-of-cell variable $S(x, y)$, as it is shown in Fig. 1(b). If the NGnet function evaluated at $S(x, y)$ features a value lower than

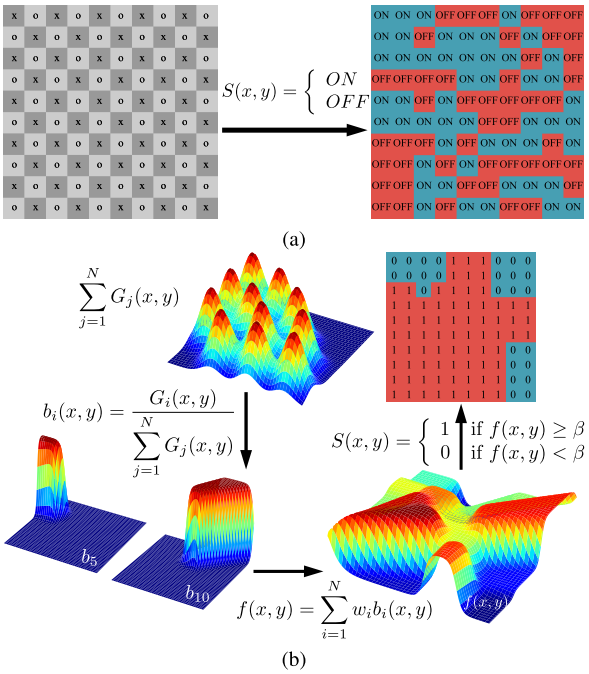

FIGURE 1. Example of TO output in the cases of (a) the ON/OFF method and (b) a NGnet defined by eleven Gaussian functions.

the pre-selected threshold β, $S(x, y)$, it is set to zero, and the material of the cell is specified as steel; if it is higher, $S(x, y)$ is defined to 1, and the assigned material is aluminum:

$$S(x,y) = \begin{cases} 1 & \text{if } f(x,y) \geq \beta \\ 0 & \text{if } f(x,y) < \beta \end{cases} . \tag{3}$$

The following section focuses on the problem of defining and implementing the TO for a case study machine.

III. ROTOR BARS OPTIMIZATION OF A LSPMSM

A. INITIAL DESIGN

For the study of bars shape using TO, a previously designed four-pole 1.5 kW LSPMSM is used. The design approach applied for the initial machine was based on retrofitting the IM rotor. The new rotor was optimized by utilizing the self-organizing migrating algorithm (SOMA), aiming for high-efficiency, power factor, and minimization of the torque ripple. Further information about SOMA can be found in [28], comparison of SOMA with more popular non-dominated sorting genetic algorithm (NSGA-II) is conducted in [29]. The design of a parametrically similar machine using the same design procedures is described in detail within [30].

Key LSPMSM geometrical parameters of the initial machine are provided in Table 1. The permanent magnet of the LSPMSM is made of neodymium-iron-boron alloy (N35H grade). The stator and rotor lamination are made from M470-50A steel, and the rotor cage aluminum alloy has a conductivity of 33 S/mm^2 at 20 °C.

TABLE 1. Key parameters of initial LSPMSM.

Parameter	Value
Rated power, kW	1.5
Pole pairs	2
Nominal frequency, Hz	50
Rated voltage line-to-line, V	400
Stator winding connection	Wye
Number of stator slots	36
Number of rotor slots	28
Active length, mm	160
Stator outer diameter, mm	135
Rotor outer diameter, mm	83
Radial air-gap length, mm	0.5

The cross-section of the reference LSPMSM can be seen in Fig. 2. The shape of the rotor bars is similar to a standard IM [31]. All rotor slots have the same geometrical shape. The stator winding is a three-phase single-layer concentric winding, and it is configured by utilizing 36 stator slots. No skewing is applied for the rotor or stator.

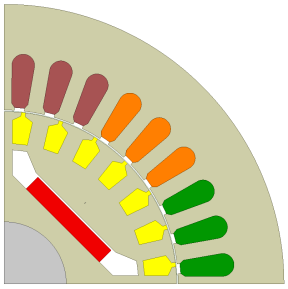

FIGURE 2. Cross-section of the initial LSPMSM.

The initial LSPMSM has been manufactured and measured to verify the used finite-element method for the presented study. The emphasis was given to verify the selected correction factor for a losses, used in machine design. The manufactured rotor of the initial LSPMSM can be seen in Fig. 3(a), and the assembled LSPMSM on the test bench is shown in Fig. 3(b).

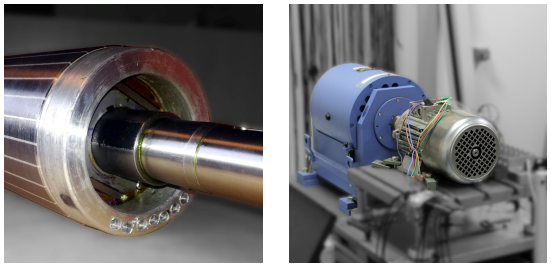

(a) (b)

FIGURE 3. Initial LSPMSM (a) rotor, and (b) measurement on the test bench.

The machine was measured, and the results are plotted and compared with the calculated ones in Fig. 4. It can be seen that the measured data correspond well to those calculated

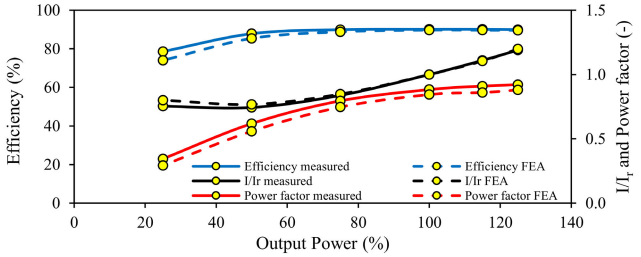

FIGURE 4. Calculated and measured performance curve comparison for the initial LSPMSM. I/I_r gives the ratio of supply current and the rated current.

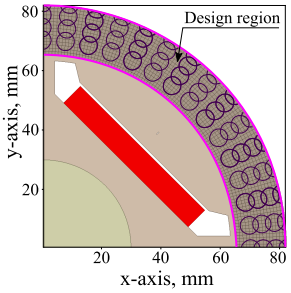

FIGURE 5. Design space discretization and deployed Gaussians used for optimization in the design region.

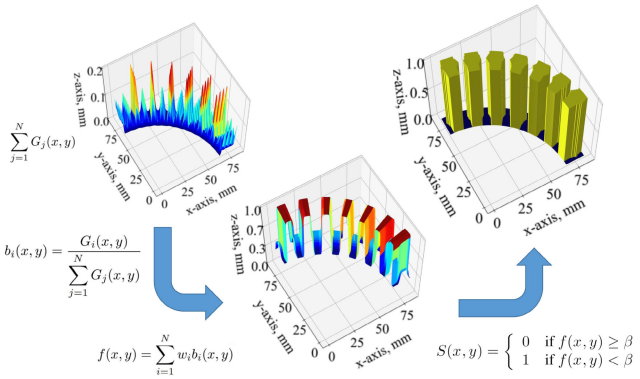

FIGURE 6. Example of Gaussians and resulting state of cell variable $S(x, y)$ within the design region. Pre-selected boundary level β is equal to 0.5.

by the FEA. The biggest difference occurs in a region corresponding to lower output power. Overall, the FEA results are more pessimistic, which might be caused by the implemented correction factor for core losses. The core losses were multiplied by a coefficient of 1.5, based on recommendations given in [31]. Besides, the extra losses, calculated as 0.5 % of the output power, were added to the total losses. Nevertheless, the results are on the safe side, and therefore the used FEA method and correction factors for initial LSPMSM are implemented in the same way within the presented research. This should ensure results close to the real, preferably on the pessimistic side.

As can be seen from the measured efficiency of 90.12 % for the rated power, the requirement for IE4 categorization was fulfilled [32]. Consequently, it can be concluded that the initial LSPMSM already features an excellent performance. This can also be attributed to the fact that the initial design has been optimized. In the subsequent sections, it is studied whether the performance of the LSPMSM can be further improved by redesigning the shape of the rotor bars through utilizing TO. The TO setup for rotor cage optimization is described in the following subsection.

B. PROBLEM SETTING

The design area for the TO is limited to the cage area. Thus, the magnet dimensions, the number of stator turns, and all other parameters of the LSPMSM remain the same as for the reference design. The model of the initial LSPMSM has been modified accordingly by replacing the cage area with a finite number of small elements ('cells'). The resultant rotor geometry with highlighted design region is shown in Fig. 5.

The number of cells in the design region is 1,515. Within this region, 60 Gaussians were deployed, as shown in Fig. 5. Gaussians were evenly positioned within the expected areas for cage bars. This approach was adopted to reduce the number of variables required to optimize. Additional reduction of design variables was achieved by the assumption of pole symmetry. Therefore, only Gaussians deployed on one half of the pole, including those in the pole center, were optimized. Thus, the total number of optimized Gaussians was 32.

The practical example of the NGnet distribution within the design region is shown in Fig. 6. Here, the NGnet is compared with pre-selected boundary level $\beta = 0.5$. Thus, the distribution of the state-of-cell variable $S(x, y)$ can be plotted for the whole design region. In areas with $S(x, y) = 1$, the assigned material will be aluminum, and conversely, areas with $S(x, y) = 0$ will be assumed to be made of steel.

C. IMPLEMENTATION

To conduct the TO of the rotor bars design, the code was developed in Python. Based on this code, the NGnet is generated, the FEA analysis is run, and post-processing and evaluation of the results is performed. The code uses Ansys Maxwell as the FEA solver. For the optimization itself, the code has been coupled with the automatized framework SyMSpace [33]. It uses the combination of elements of differential evolution (DE) and Strength Pareto Evolutionary Algorithm 2/Non-dominated Sorting Genetic Algorithms II (SPEA2/NSGA-II) during the optimization run [34]. SyMSpace is developed by the Linz Center of Mechatronics and the Department of Electric Drives and Power Electronics at Johannes Kepler University, Linz.

The developed methodology of the design evaluations during the optimization is shown in Fig. 7. The procedure of evaluation is done in such a way as to minimize the number of unsuitable geometries before performing time-consuming transient simulations, with voltage sources. First, SyMSpace framework provides sets of Gauss weighting coefficients during the optimization. Then, the developed code computes the NGnet, and the geometry is generated and set in Ansys Maxwell.

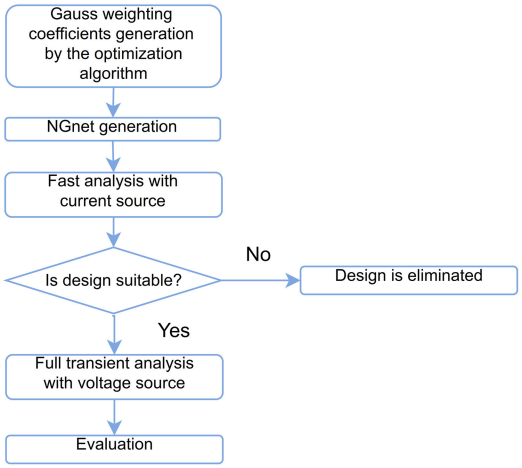

FIGURE 7. Methodology of evaluation for one individual design.

Subsequently, the design is simulated by magnetic time-transient analysis with a current source. This allows to distinguish between geometries, providing poor and sufficient performance in a very short time. During this analysis, the torque ripple and average value of the machine electromagnetic torque are observed. If both observed variables are in the desired range, the evaluation continues with analysis with voltage sources. If not, then the design is not considered for further analyses.

Suitable designs from the initial step are then evaluated by magnetic time-transient analysis. Throughout this analysis, the machine is supplied from a voltage source providing nominal line-to-line RMS voltage of 400 V. The machine is loaded with the rated torque of 9.55 Nm and started from zero speed to allow observation of the synchronization capabilities of the design. The motion equation for this analysis is set so that damping correlates to the mechanical losses, and the mass of inertia of the load equals the rotor inertia multiplied by five.

For the sake of simplicity, the moment of inertia of the rotor is not recalculated separately for each optimized design but is considered the same as that observed for the manufactured initial LSPMSM. The determined moment of inertia is 0.00593 kg.m^2, and it is considered not to be appreciably affected by simply changing the shape of the cage in a limited area of the design region as in shown in Fig. 5.

Only designs capable of synchronization with the mentioned conditions are considered for further post-processing. This should ensure that the starting performance of the optimized design will be in line with commercially available LSPMSMs, e.g. [35]. After this simulation, the design is evaluated, and results are used for further optimization by the framework.

The optimization goals are maximization of the efficiency, power factor, and reduction of the torque ripple. At the same time, the design has to be capable of synchronizing the nominal load with an inertia five times larger than that of the LSPMSM rotor. Due to these objectives being conflicting, the outcome of the optimization is a Pareto front which is presented in the following section.

IV. RESULTS

A. OPTIMIZATION

During the optimization, approximately 35,400 of almost of 43,500 designs, were evaluated by full transient analysis with voltage source. The Pareto-optimal designs for optimal design parameters are shown in Fig. 8. The Pareto curve illustrates achievable torque ripple and power factor versus efficiency. For a 1.5 kW four-pole machine in the IE4 efficiency class, the required efficiency is at least 88.2 % [32]. It can be seen from the results in Fig. 8 that designs are available in the IE4 efficiency class, even with a sufficient margin. The highest efficiencies of the optimized designs are slightly above 91.7 %. The reference machine featured an estimated efficiency of 89.7 % by using FEA.

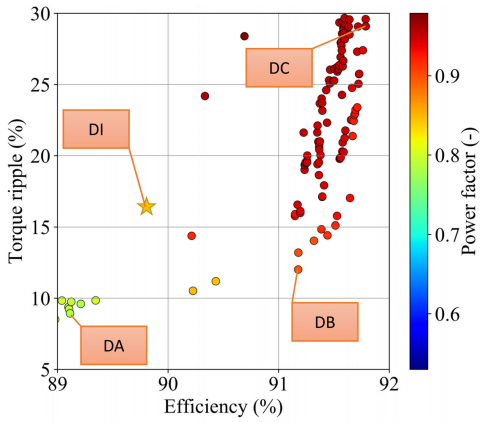

FIGURE 8. Pareto-optimal results for torque ripple vs. efficiency and power factor.

Three optimized designs were selected for further study and detailed comparison with the reference machine and are marked as: Design A (DA), Design B (DB), and Design C (DC) in Fig. 8. The first selected design, DA, has the low torque ripple and, at the same time, sufficient efficiency for the IE4 efficiency class. The second resultant geometry, DB, has some sort of compromise between the efficiency of all studied machines and torque ripple. Lastly, DC is selected as the design with the highest efficiency but also torque ripple. The initial design (DI), presented in Section III, is also marked in Fig. 8 by a small yellow star. It can be seen that DI is not too far from the Pareto-optimal curve.

The resulting geometries of the selected optimized machines are shown in Fig. 9 and their corresponding normalized Gaussians networks and states of cell variables $S(x, y)$ in Fig. 10. DA, as shown in Fig. 9(a), has a similar pole shape to a salient pole separately excited synchronous machine [31], with the difference that the excitation is provided by permanent magnets in a LSPMSM. The other two designs, Fig. 9(b) and (c), have more classical geometry, with several

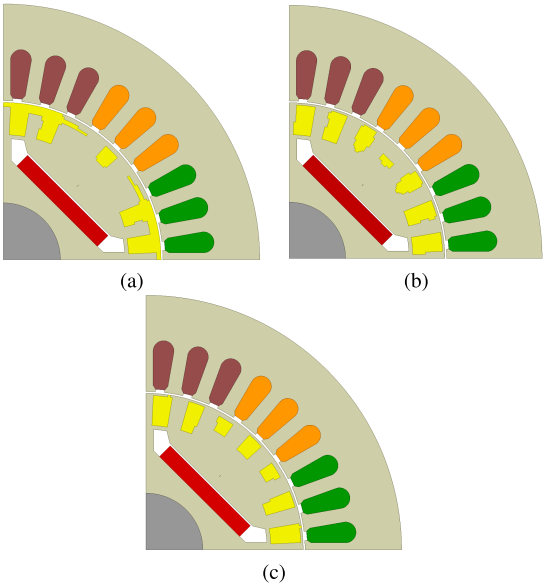

FIGURE 9. Cross-sections of the selected machine designs: (a) Design DA, (b) Design DB, and (c) Design DC.

slots for their rotor cage. In general, the resulting shapes of the rotor bars in the optimized designs DB and DC are predominantly angular. This is caused by the number of Gaussians used for optimization. Smoother rotor bar geometries could probably be achieved if more Gaussians were deployed within the design region. On the other hand, this would increase the already high number of design parameters.

The optimized cage slots illustrated for DB and DC in Fig. 9(b) and (c) are asymmetrical. This means that the resistance of the cage in the d-axis is not the same as that in the q-axis. The resistance of the cage in the d-axis is mainly defined by bars located in the q-axis; conversely, the resistance of the cage in the q-axis is mainly defined by the shape of the bars in the d-axis [6]. According to [6], the LSPMSM can benefit in terms of cage torque from this asymmetry. For the optimized designs DB and DC, the bar surfaces in the d-axis are not as big as the q-axis bar equivalents.

The electromagnetic performance of the optimized geometries is evaluated and compared with the initial design DI for rated load and no-load conditions in the following subsections. The starting performance is also studied.

B. RATED-LOAD PERFORMANCE

The calculated steady-state performance of the optimized machines is compared with the initial one in Table 2. In this table, the design performances were calculated with a finer discretization than the step size used for the optimization. Specifically, 100 steps per period were used for optimization, while the results in Table 2 were calculated with 200 steps per period. The refinement should provide more accurate results, while the coarser step for the optimization run was chosen to save time. This led to a slight difference between the results presented in Table 2 and Fig. 8. The main difference relates to the presented torque ripple value, while the efficiency values almost match.

As can be seen in Table 2, except for DA, the optimized designs have more than 1 % higher efficiency, in absolute value, than DI. This can be considered as a significant improvement for a given machine rated power of 1.5 kW. Moreover, all designs have lower torque ripple compared to the DI, excluding DC. The higher efficiency correlates to the higher power factor of DB and DC. The improvement of the

TABLE 2. Rated performance comparison.

Parameter	DI	DA	DB	DC
Output power, W	1511	1506	1535	1526
Torque, Nm	9.6	9.6	9.7	9.7
Current, A	2.7	3.0	2.6	2.4
Efficiency, %	89.7	89.2	91.1	91.8
Power factor, -	0.86	0.78	0.91	0.96
Torque ripple, %	16.50	8.90	15.73	24.92
Saliency ratio L_q/L_d, -	5.21	2.17	6.00	4.22

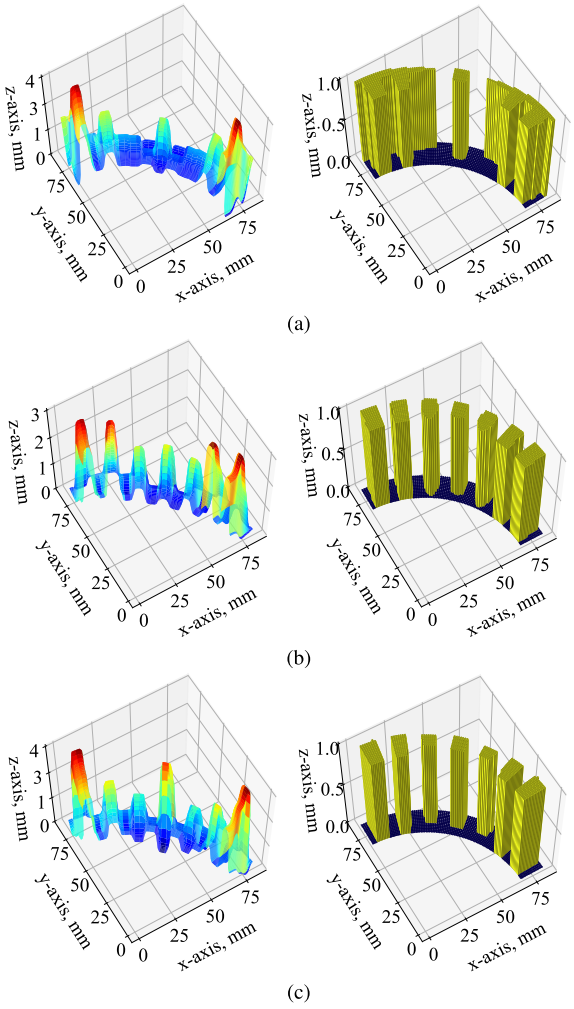

FIGURE 10. Normalized Gaussians networks for the selected machine designs (left) and resulting states of cell variables $S(x, y)$ (right) within the design region: (a) Design DA, (b) Design DB, and (c) Design DC. Pre-selected boundary level β is equal to 0.5.

power factor can be explained by an increase of the no-load induced Back-EMF shown within the following subsection in Table 5. The LSPMSM behaves similar to a synchronous machine connected to the infinite bus. Thus, the change of the no-load induced Back-EM signifies a change of power factor. The presented designs are under-excited, and thus, current is lagging. The stator current is minimum when the no-load induced Back-EMF is roughly equal to the mains voltage. In contrast, a higher Back-EMF reduces the machine's ability to successfully start [5].

A better understanding of efficiency improvement for DB and DC is provided by the loss comparison shown in Table 3: the higher power factor of the optimized designs leads to a smaller current (Table 2), which results in lesser stator resistive losses. The core losses are lower for all optimized designs. The provided results are modified by manufacturing coefficient and extra losses in the same way as for the initial machine presented in Section III.

TABLE 3. Losses comparison.

Parameter	DI	DA	DB	DC
Stator resistive losses, W	95.9	112.0	80.8	67.8
Core Losses, W	53.0	44.9	44.8	43.5
Rotor resistive losses, W	5.0	15.1	5.5	5.6
Mechanical losses, W	12	12	12	12
Extra losses, W	7.6	7.5	7.7	7.6
Total losses, W	173.5	182.8	150.8	136.5

Another important parameter of the LSPMSM is the saliency ratio, defined as the q-axis inductance L_q divided by d-axis inductance L_d. The saliency ratio, and the Back-EMF E_f affect the machine's overall efficiency and power factor. It can be seen from Table 2 that DB has the highest saliency ratio, followed by DI. DA features the smallest saliency ratio. This is expectable based on the rotor geometry shown in Fig. 9(a).

The per unit (p.u.) inductances of each design, along with other selected p.u. parameters, can be found in Table 4. Per unit, values are obtained by dividing each value by a base value. Peak values of rated phase current and rated voltage of the machine are selected as the base value for the current and the voltage, respectively. The base value of inductance is estimated as the peak value of the rated phase voltage divided by the product of rated angular speed and the peak value of the rated phase current. The rated phase current is assumed to be equal to the current of the individual design listed in Table 2.

Geometry DC has the highest inductance of all designs, and the inductance of DA is quite low compared to the other designs, as is its saliency ratio. This results in a smaller reluctance torque component in the total torque of DA. Therefore, the current needed to power DA in order to deliver nominal torque is higher than that for the other designs, and the efficiency is lower as a consequence of increased stator winding resistive losses, which are listed in Table 3.

At the same time, DA exhibits rotor resistive losses representing 8.26 % of the total losses, which is the highest proportion of these losses compared to the other variants. For the rest of the variants, the losses are close to 3 %. The higher rotor resistive losses of DA can be explained by its cage shape, which is more prone to the higher harmonic components of the magnetic flux density in the air-gap. This results in the induction of a higher voltage during synchronous operation and consequently higher losses compared to those of the other designs.

The parameters presented in Table 4, together with the results of the FEA, are used to plot the vector diagrams shown in Fig. 11. The small inductance of design DA results in relatively small quadrature axis reaction, Fig. 11(b). On contrary, the quadrature axis reaction is significant in other designs. The highest quadrature axis flux linkage is observed for DI, followed by DC. The load angle is within the range 40° – 46° for DI, DB, and DC. This ensures sufficient torque overload capabilities. The lowest load angle can be observed for DA.

TABLE 4. Selected d- and q- axis components as per unit values.

Parameter	DI	DA	DB	DC
I_d, p.u.	-0.27	0.32	-0.26	-0.45
I_q, p.u.	0.96	0.95	0.97	0.89
U_d, p.u.	-0.69	-0.32	-0.61	-0.66
U_q, p.u.	0.67	0.9	0.74	0.74
L_d, p.u.	0.14	0.17	0.11	0.18
L_q, p.u.	0.73	0.37	0.66	0.76

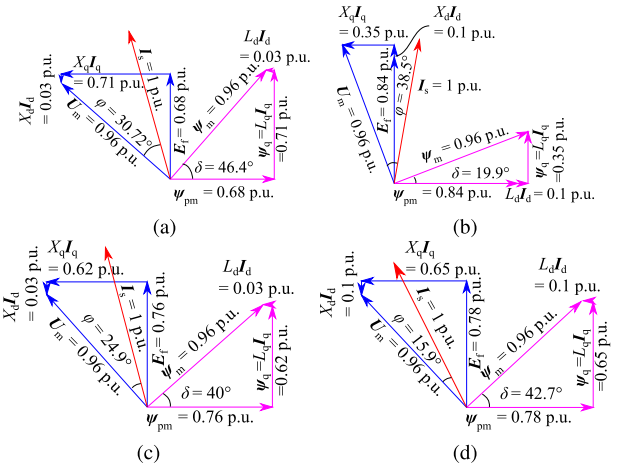

FIGURE 11. Vector diagram for (a) the reference machine, (b) Design A, (c) Design B, and (d) Design C. Here, ψ_m corresponds to air-gap flux linkage and ψ_q is quadrature axis flux linkage excited by product of quadrature axis inductance L_q and current I_q. The Back-EMF E_f is induced by the permanent magnet flux linkage ψ_{pm} created by the permanent magnets located in the rotor. The leakage inductance and resistance of the stator winding is neglected in the plotted vector diagram. Nevertheless, the voltage drop on stator winding resistance and leakage inductance can be seen on the value of magnetizing voltage U_m.

The strong quadrature axis reaction of DI, DB, and DC can be seen in the flux density plots presented in Fig. 12(a), (c), and (d), respectively. The DA flux density plot can be found in Fig. 12(b). As a result of closed rotor slots

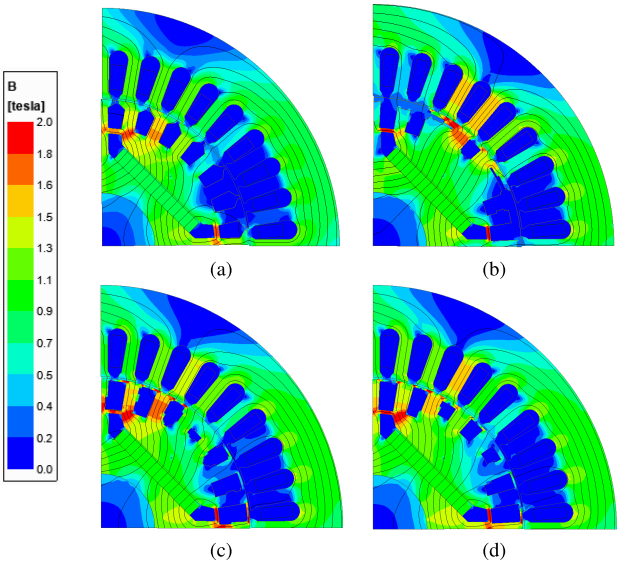

FIGURE 12. Magnetic flux distribution at the rated operating point for (a) the reference machine DI, (b) Design DA, (c) Design DB, and (d) Design DC.

in the optimized designs, the air-gap flux density has smaller pulsation due to the rotor slotting. This results in smaller core losses when compared to the reference machine, as shown in Table 3. Fig. 12 shows that the largest saturated areas occur in the design DB around the rotor slots.

The torque characteristics for steady-state operation, including corresponding harmonic spectra, are shown in Fig. 13. The largest harmonics in the torque are 6, 12 and 18, corresponding to 300, 600 and 900 Hz, respectively. These harmonics are caused by the interaction of the harmonic field produced by the stator and field generated by the permanent magnets.

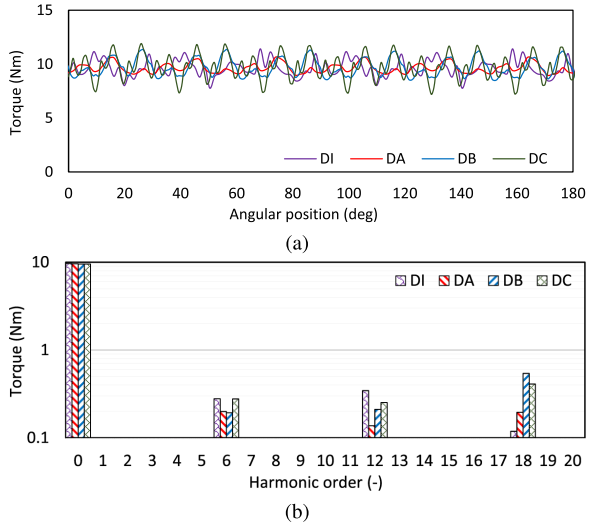

FIGURE 13. Comparison of (a) the torque dependencies versus angular rotor position during steady-state operation and (b) corresponding harmonic spectra.

C. NO-LOAD PERFORMANCE

First, the no-load condition is observed with stator winding disconnected from the supply at the synchronous speed of 1,500 rpm. This allows the no-load Back-EMF and permanent magnet flux linkage to be estimated The induced no-load Back-EMF for all designs is listed in Table 5. It can be seen that DA features the highest E_f. Moreover, DB and DC have a higher induced voltage than DI. To study this difference further, the no-load voltage and flux density waveform, together with corresponding harmonic spectrum, are plotted in Fig. 14 and Fig. 15, respectively.

TABLE 5. No-load performance at rated speed of 1500 rpm.

Parameter	DI	DA	DB	DC
Induced no-load Back-EMF, V	157	192	174	179
Air-gap flux density, the fundamental, T	0.49	0.57	0.52	0.53

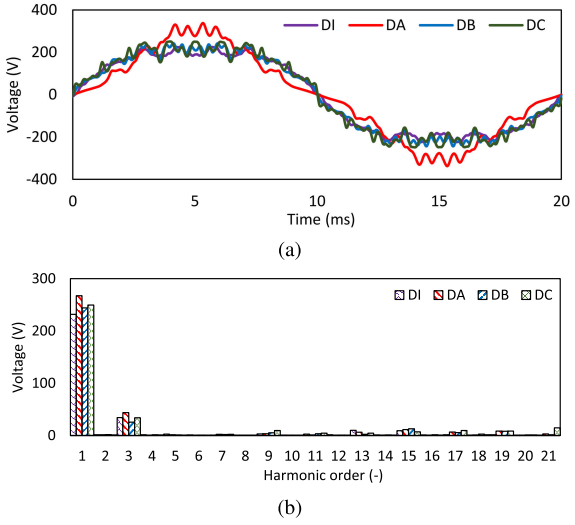

FIGURE 14. Comparison of (a) the no-load induced voltage (Back-EMF) waveform and (b) corresponding harmonic spectrum.

The fundamental is the dominant component of air-gap flux density harmonics for all designs. Their respective values are listed in Table 5. The next in magnitude are the third harmonic component, related to a rectangular wave shape of air-gap flux density, and first-order stator slot harmonics, particularly the seventeenth and nineteenth harmonic order. In contrast, the first-order, thirteenth and fifteenth harmonic orders of the rotor are smaller.

The harmonic spectrum of the induced voltage is defined by the winding configuration and corresponding winding factors for individual harmonic orders, which 'filter' some of the air-gap flux density harmonic components. The highest first- and third-order harmonics of the flux density and induced voltage are observed for DA. In contrast, DB has the lowest first- and third-order harmonics. Nevertheless, apart from DA, all other designs have similar waveforms.

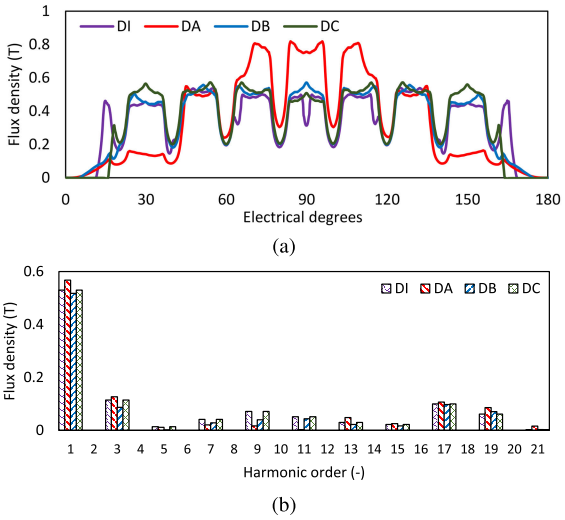

FIGURE 15. Comparison of (a) the flux density in the middle of the air–gap, and (b) the corresponding harmonic spectrum. The average value of magnetic flux density over one pole pitch for design DI, DA, DB, and DC is 0.33, 0.33, 0.34, and 0.35 T, respectively.

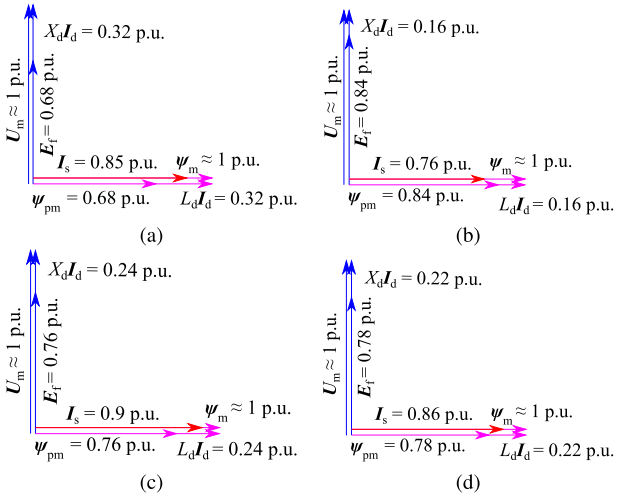

FIGURE 17. Vector diagram for grid connected machines operating at no-load: (a) the initial design DI, (b) Design DA, (c) Design DB, and (d) Design DC.

The no-load air-gap flux density distribution of the optimized designs is compared with the initial machine counterpart in Fig. 16. For all designs, the thin bridge separating the cage slot from the magnet cavity is saturated. In addition, the pole head is saturated in DA.

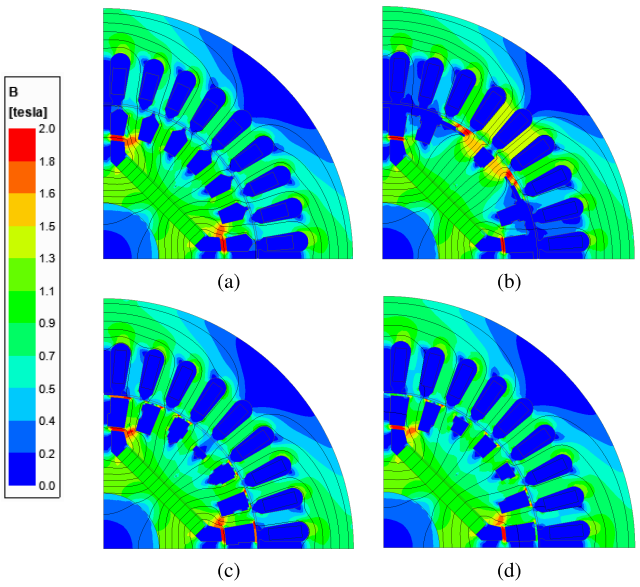

FIGURE 16. Magnetic flux distribution at the no-load operation for (a) the initial design DI, (b) Design DA, (c) Design DB, and (d) Design DC.

Lastly, the no-load operation of the grid-connected LSPMSM is studied. With a light load, the air-gap flux of LSPMSMs tends to increase, because of a lower voltage drop on leakage reactance. The vector diagrams of this no-load operation for each design are shown separately in Fig. 17. It can be seen that the no-load current is quite high. Therefore, the efficiency of the LSPMSM compared with the classical IM can even be lower for light load operations.

The individual flux linkages for grid-connected no-load operations are shown in Fig. 18. From this figure, it is possible to see the total flux in the air gap and the magnitude of the flux contribution from the magnet itself. This portion is also clearly visible for rated-load operation in the vector diagrams, as illustrated in Fig. 11. From these results, it can be seen that the permanent magnet flux linkage strongly affects the machine's power factor considering the presented LSPMSM designs.

D. STARTING PERFORMANCE

Lastly, the starting performance is compared for the optimized designs. According to [5], the LSPMSM starting capability is limited by permanent magnet braking torque, cage torque, and reluctance torque due to the machine saliency. As a result, there is a limited amount of load torque that can be synchronized for a given inertia. The curve of inertia dependency on load torque, which defines the load that the machine is able to synchronize, is called synchronizing capability [5]. These curves are plotted for the studied machines in Fig. 19. Loads higher than the limit given by the respective curve cannot be synchronized by the corresponding LSPMSMs.

From Fig. 19, it can be observed that the synchronizing capability of the initial machine is better than that of the optimized designs. This is because of the increase in permanent magnet flux linkage ψ_{pm} in the optimized designs, and the cross-section reduction of the rotor bars. As a result, the optimized machine has a higher magnet braking torque, which reduces its starting capability. Moreover, a smaller rotor bars cross-section decreases the torque/speed curve gradient near the synchronous speed. This leads to a further reduction of the synchronization capability of the LSPMSM [5]. Nonetheless, the starting capabilities of the optimized designs are

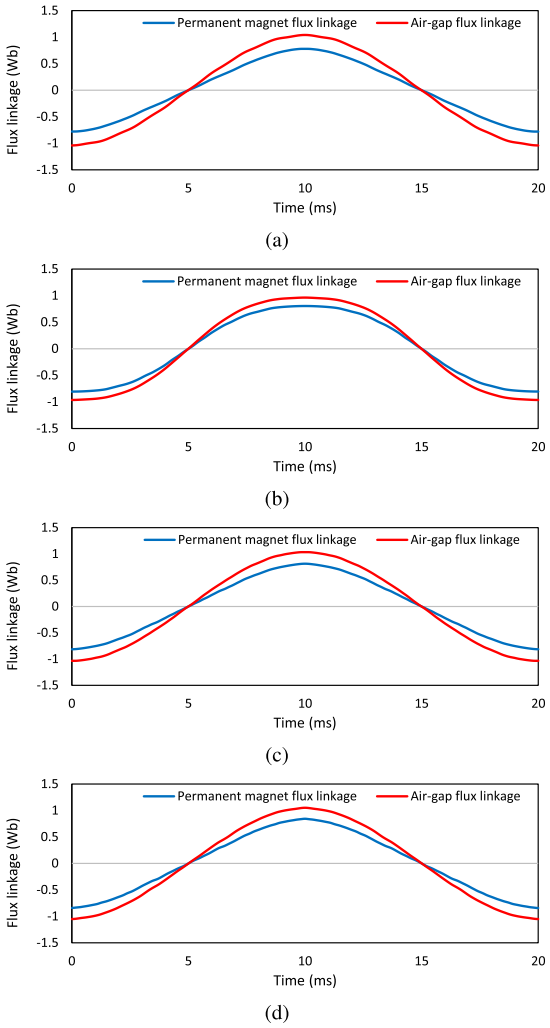

FIGURE 18. Permanent magnet and air-gap flux linkage of the grid-connected machines operated with no-load: (a) the initial design DI, (b) design DA, (c) design DB, and (d) design DC.

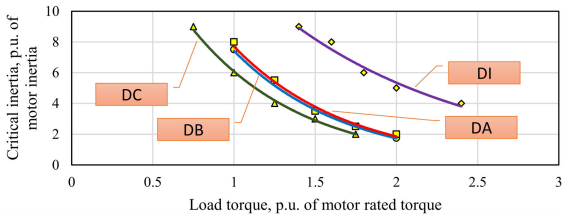

FIGURE 19. Synchronization capability curve for the reference and the optimized machine.

still acceptable and can provide a reasonable trade-off when taking into account their improved steady-state performance.

Torque and speed during the run-up can be found in Fig. 20. The time required for starting is almost the same for all compared designs. During the starting process, the torque strongly oscillates and, therefore, has the potential to generate high stress on the coupling. The imposed load torque at which start-up analysis is performed is equal to the machine's rated torque of 9.55 Nm, and the moment of inertia is the one

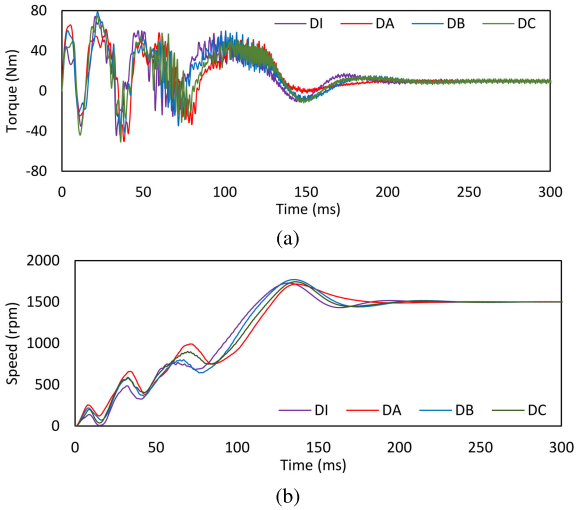

FIGURE 20. Comparison of (a) the torque dependencies versus time, and (b) the speed dependency vs. time during run-up with rated load for all investigated designs.

determined by measurements on the manufactured DI, equal to 0.00593 kg.m^2 and multiplied by two to consider the inertia of the load. In other words, the moment of inertia of DI is used for equitable comparison of all presented designs. This simplification can be justified on the basis that the inertia of the individual designs does not widely vary, with the only difference being the amount of aluminum on the rotors within a limited area.

The torque waveform of the machines during start-up shown in Fig. 20(a) has relatively strong pulsations. In certain time instants, the total machine torque is even negative, and therefore lower than the constant load torque applied, causing the speed to drop (Fig. 20(b)). Consequently, in a short period of time, the rotational speed changes its value around a mean value lower than the synchronous speed, hence giving the appearance of a crawling effect. To study this briefly, the total torque given in Fig. 20 was decomposed into permanent magnet, reluctance, and cage torque components. The decomposition into components is based on the following torque equation:

$$T = T_{\mathrm{pm}} + T_{\mathrm{rel}} + T_{\mathrm{cage}}, \tag{4}$$

where T_{pm} is the magnet torque component, T_{rel} is the reluctance torque component, and T_{cage} is the cage torque component. The separation into components was achieved by computing the magnet torque and subtracting it from the total torque. This resulted in a component corresponding to the sum of the reluctance and the cage torque. The permanent magnet torque was calculated by the following equation:

$$T_{\mathrm{pm}} = \frac{3}{2}\psi_{\mathrm{pm}} i_{\mathrm{q}}. \tag{5}$$

For the sake of simplicity, the permanent magnet flux linkage of each design was taken from the no-load analysis presented in Section IV-C. Therefore, the implemented

decomposition into components neglects the change in magnetic circuit saturation during start-up. Even so, the results provide a clearer understanding of the phenomena.

The resultant waveforms for torque decomposition are shown for each design separately in Fig. 21. The permanent magnet torque oscillates with a frequency given by the product of the slip and supply frequency of the machine. A pulsating torque with this frequency can also be seen in Fig. 20(a). It can also be stated that the amplitudes of the pulsating torques are mainly based on the permanent magnet flux linkage. Further, the provided waveforms show that the average magnet torque component during acceleration is negative, and the sum of the average reluctance and cage torque is positive. Thus, the sum of the average reluctance and cage torque allows for rotor acceleration, whereas the magnet torque acts as a brake. After synchronization, in the designed machines, the permanent magnet creates a dominant torque component.

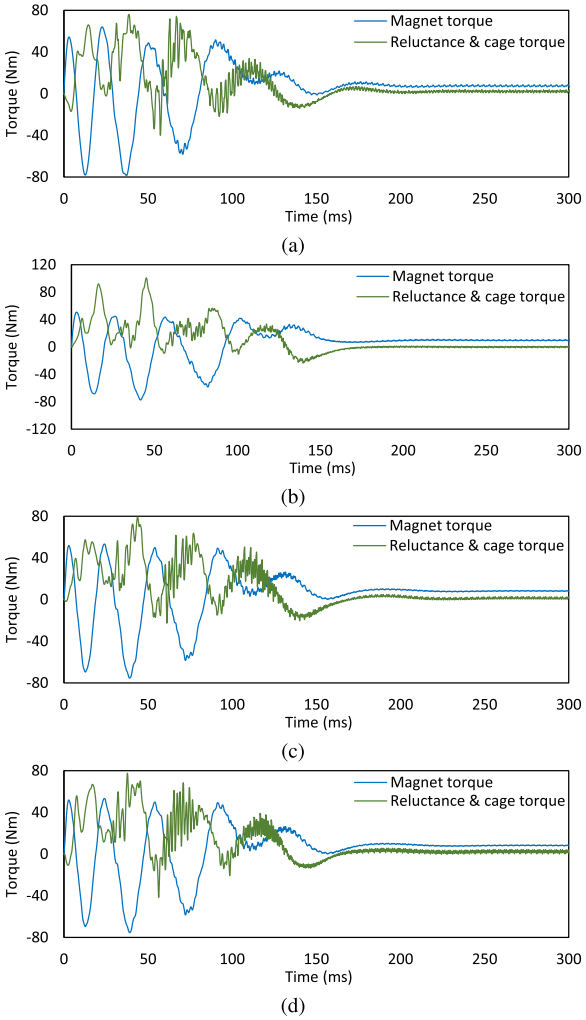

FIGURE 21. Computed torque components versus time during run-up: (a) the initial design DI, (b) design DA, (c) design DB, and (d) design DC.

The LSPMSM starting phenomenon is a very complex matter, and a more detailed analysis together with optimization of the machine in order to minimize oscillations during start-up is beyond the scope of this paper.

V. DISCUSSION OF MANUFACTURABILITY

In the previous Section IV, simulation results for all three optimized machine designs were shown. Although these machines were not manufactured within the presented research, this section aims to provide a short discussion of their manufacturability based on experience with DI production.

As discussed in Section II, the advantage of TO based on NGnet is that it tends to provide manufacturable geometries. Even so, before manufacturing, the rotor lamination geometry would have to be modified to consider manufacturability requirements. One of the main risks is a leak of the aluminum alloy during die casting to the magnet cavity. As the production of the DI version has revealed, the cage die casting of a machine with an axial stack length of 160 mm is challenging. Because of this, it may be necessary to provide a specific form for die casting such rotors, designed to avoid aluminum penetrating the magnet cavity as much as possible.

Similar to the DI, the DB and DC designs can be produced using a combination of modified rotor cover lamination Fig. 22(b) and complete forms optimized for the designed rotor geometries. Radiuses in the rotor slots edges of DB and DC would have to be introduced before production. Furthermore, the outer diameter of the rotor should be supported by a suitable form during the die casting process to prevent deformation. This is because of the thin bridges near the rotor surface. Another countermeasure to prevent deformation would be die casting of lamination with a larger outer diameter that would later be machined.

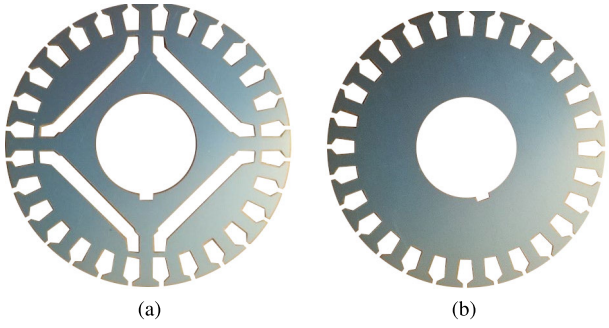

FIGURE 22. Lamination used to fabricate design DI: (a) the lamination for active stack part, (b) cover lamination. The cover lamination prevents aluminum to leak into the magnet cavity, and it is removed after die casting. Similarly, design DB and DC can be produced.

From the optimized geometries shown in Fig. 9, it is clear that the manufacturability of the DA design is considerably more problematic compared to the DB and DC designs. That is due to the large uniform aluminum region near the rotor surface. Similar to DB and DC, for the production of design DA, the lamination would have to be prepared with a sufficiently larger outer diameter to avoid undesirable deformations during the squirrel-cage die casting. After casting, the addition to the outer surface would have to be machined

away. Nevertheless, the DA design would still require a careful check of the mechanical rigidity of the rotor structure and resistance to centrifugal force before actual manufacture. However, this analysis is beyond the scope of this paper.

VI. CONCLUSION

This paper has presented a study of the rotor bar geometry and arrangement of a line-start permanent magnet synchronous machine using topology optimization. The employed topology optimization method was based on a normalized Gaussian network. Only the cage area of the rotor was considered for the optimization. The permanent magnet and respective slot dimensions were adopted from a previous machine design rated in the IE4 efficiency class. To verify the adopted FEA based approach, the electromagnetic model of the initial machine has been verified by measurements conducted for a manufactured prototype. The comparison showed that FEA gives more pessimistic results compared to reality, and the electromagnetic model consequently has a sufficient safety margin.

The optimization was conducted by using the automatized framework SyMSpace coupled with Python scripts with Ansys Maxwell. The optimization results were presented, and three designs were selected for further detailed analyses and a comparison with the initial design. The first one features a small torque ripple, and efficiency close to the border of the IE4 efficiency class. The second one provides higher efficiency and torque ripple, and the third features the highest efficiency and torque ripple.

The optimized machine designs have a smaller bar height in the *d*-axis of the rotor pole region; thus, the permanent magnet flux linkage is increased. Another difference compared to the initial machine is that the optimized designs have closed rotor slots. The study reveals that machines with a modified rotor bar shape achieved better steady-state performance than the initial machine. The presented work provided rated-load, no-load, start-up, and transient comparisons.

The obtained results suggest that further improvement of LSPMSM parameters is possible by implementing a non-uniform rotor cage bars shape. The conducted research can be further enhanced by a higher emphasis on the starting performance within the optimization. Further improvement could be achieved with more deployed Gaussians within the design region and by further considering the magnet dimensions as design parameters for the optimization.

The presented research results provide new insights into LSPMSMs design. Its conclusions can be used for future research and development of LSPMSMs for a wide range of applications.

REFERENCES

[1] R. T. Ugale, B. N. Chaudhari, and A. Pramanik, "Overview of research evolution in the field of line start permanent magnet synchronous motors," *IET Electr. Power Appl.*, vol. 8, no. 4, pp. 141–154, Apr. 2014.

[2] A. T. de Almeida, F. J. T. E. Ferreira, and G. Baoming, "Beyond induction motors—Technology trends to move up efficiency," *IEEE Trans. Ind. Appl.*, vol. 50, no. 3, pp. 2103–2114, Jun. 2014.

[3] A. T. de Almeida, F. J. T. E. Ferreira, and A. Quintino Duarte, "Technical and economical considerations on super high-efficiency three-phase motors," *IEEE Trans. Ind. Appl.*, vol. 50, no. 2, pp. 1274–1285, Mar. 2014.

[4] T. Marcic, B. Stumberger, and G. Stumberger, "Comparison of induction motor and line-start IPM synchronous motor performance in a variable-speed drive," *IEEE Trans. Ind. Appl.*, vol. 48, no. 6, pp. 2341–2352, Nov. 2012.

[5] J. R. Hendershot and T. J. E. Miller, *Design of Brushless Permanent-Magnet Machines* (Motor Design Books LLC). USA: Motor Design Books LCC, 2010.

[6] I. Boldea and L. Tutelea, *Reluctance Electric Machines: Design and Control*. Boca Raton, FL, USA: CRC Press, 2018.

[7] L. S. Maraaba, Z. M. Al-Hamouz, and M. A. Abido, "An accurate tool for detecting stator inter-turn fault in LSPMSM," *IEEE Access*, vol. 7, pp. 88622–88634, 2019.

[8] L. S. Maraaba, A. S. Milhem, I. A. Nemer, H. Al-Duwaish, and M. A. Abido, "Convolutional neural network-based inter-turn fault diagnosis in LSPMSMs," *IEEE Access*, vol. 8, pp. 81960–81970, 2020.

[9] L. S. Maraaba, Z. M. Al-Hamouz, A. S. Milhem, and M. A. Abido, "Neural network-based diagnostic tool for detecting stator inter-turn faults in line start permanent magnet synchronous motors," *IEEE Access*, vol. 7, pp. 89014–89025, 2019.

[10] D. Mingardi, N. Bianchi, and M. Dai Prè, "Geometry of line start synchronous motors suitable for various pole combinations," *IEEE Trans. Ind. Appl.*, vol. 53, no. 5, pp. 4360–4367, Oct. 2017.

[11] R. T. Ugale and B. N. Chaudhari, "Rotor configurations for improved starting and synchronous performance of line start permanent-magnet synchronous motor," *IEEE Trans. Ind. Electron.*, vol. 64, no. 1, pp. 138–148, Jan. 2017.

[12] R. T. Ugale, B. N. Chaudhari, S. Baka, S. S. Dambhare, and A. Pramanik, "Induced pole rotor structure for line start permanent magnet synchronous motors," *IET Electr. Power Appl.*, vol. 8, no. 4, pp. 131–140, Apr. 2014.

[13] T. Ding, N. Takorabet, F. M. Sargos, and X. Wang, "Design and analysis of different line-start PM synchronous motors for oil-pump applications," *IEEE Trans. Magn.*, vol. 45, no. 3, pp. 1816–1819, Mar. 2009.

[14] K. Kurihara and M. A. Rahman, "High-efficiency line-start interior permanent-magnet synchronous motors," *IEEE Trans. Ind. Appl.*, vol. 40, no. 3, pp. 789–796, May 2004.

[15] O. Ustun, D. Bayram, B. Durak, and O. C. Kivanc, "Comparison of different line start interior permanent magnet synchronous motor types with respect to IE4 efficiency class," in *Proc. 18th Int. Symp. Electromagn. Fields Mechatronics, Elect. Electron. Eng. (ISEF) Book Abstr.*, Sep. 2017, pp. 1–2.

[16] S. Saha, G.-D. Choi, and Y.-H. Cho, "Optimal rotor shape design of LSPM with efficiency and power factor improvement using response surface methodology," *IEEE Trans. Magn.*, vol. 51, no. 11, pp. 1–4, Nov. 2015.

[17] B. M. Dinh, "Optimal rotor design of line start permanent magnet synchronous motor by genetic algorithm," *Adv. Sci., Technol. Eng. Syst. J.*, vol. 2, no. 3, pp. 1181–1187, Jul. 2017. [Online]. Available: http://astesj.com/v02/i03/p149/

[18] M. M. Ghahfarokhi, A. D. Aliabad, S. T. Boroujeni, E. Amiri, and V. Z. Faradonbeh, "Analytical modelling and optimisation of line start LSPM synchronous motors," *IET Electr. Power Appl.*, vol. 14, no. 3, pp. 398–408, 2020. [Online]. Available: https://ietresearch.onlinelibrary.wiley.com/doi/abs/10.1049/iet-epa.2019.0644

[19] M. Lin, D. Li, Y. Zhao, X. Ren, and R. Qu, "Improvement of starting performance for line-start permanent magnet motors by winding reconfiguration," *IEEE Trans. Ind. Appl.*, vol. 56, no. 3, pp. 2441–2450, May 2020.

[20] A. D. Aliabad, M. Mirsalim, and N. F. Ershad, "Line-start permanent-magnet motors: Significant improvements in starting torque, synchronization, and steady-state performance," *IEEE Trans. Magn.*, vol. 46, no. 12, pp. 4066–4072, Dec. 2010.

[21] J. Fu, J. Huang, and J. Liu, "Topology optimization with selective problem setups," *IEEE Access*, vol. 7, pp. 180846–180855, 2019.

[22] Y. Hu, Y. Xiao, B. Chen, and Q. Li, "Topology optimization of a consequent-pole rotor with V-shaped magnet placement," in *Proc. 21st Int. Conf. Electr. Mach. Syst. (ICEMS)*, Oct. 2018, pp. 234–239.

[23] Y. Sun Kim and I. Han Park, "Topology optimization of rotor in synchronous reluctance motor using level set method and shape design sensitivity," *IEEE Trans. Appl. Supercond.*, vol. 20, no. 3, pp. 1093–1096, Jun. 2010.

[24] S. Sato, T. Sato, and H. Igarashi, "Topology optimization of synchronous reluctance motor using normalized Gaussian network," *IEEE Trans. Magn.*, vol. 51, no. 3, pp. 1–4, Mar. 2015.

[25] T. Ishikawa, K. Nakayama, N. Kurita, and F. P. Dawson, "Optimization of rotor topology in PM synchronous motors by genetic algorithm considering cluster of materials and cleaning procedure," *IEEE Trans. Magn.*, vol. 50, no. 2, pp. 637–640, Feb. 2014.
[26] Y. Okamoto, Y. Tominaga, S. Wakao, and S. Sato, "Topology optimization of rotor core combined with identification of current phase angle in IPM motor using multistep genetic algorithm," *IEEE Trans. Magn.*, vol. 50, no. 2, pp. 725–728, Feb. 2014.
[27] T. Sato, K. Watanabe, and H. Igarashi, "Multimaterial topology optimization of electric machines based on normalized Gaussian network," *IEEE Trans. Magn.*, vol. 51, no. 3, pp. 1–4, Mar. 2015.
[28] I. Z. D. Davendra, *Self-Organizing Migrating Algorithm*. Cham, Switzerland: Springer, 2016.
[29] L. Knebl, J. Barta, G. Bramerdorfer, O. Vitek, and C. Ondrusek, "Multi-objective optimization of a line-start synchronous machine using a self-organizing algorithm," *IEEE Trans. Magn.*, vol. 57, no. 6, pp. 1–4, Jun. 2021.
[30] J. Barta, L. Knebl, M. Toman, V. Abramenko, I. Petrov, and I. Lolova, "Design and analysis of 1.5 kW, 1500 rpm line-start permanent magnet synchronous machine," in *Proc. 19th Int. Conf. Mechatronics-Mechatronika (ME)*, Dec. 2020, pp. 1–5.
[31] J. Pyrhönen, T. Jokinen, and V. Hrabovcova, *Design of Rotating Electrical Machines*. Hoboken, NJ, USA: Wiley, 2013.
[32] A. T. De Almeida, F. J. T. E. Ferreira, and J. A. C. Fong, "Standards for efficiency of electric motors," *IEEE Ind. Appl. Mag.*, vol. 17, no. 1, pp. 12–19, Jan./Feb. 2011.
[33] S. Silber, W. Koppelstatter, G. Weidenholzer, G. Segon, and G. Bramerdorfer, "Reducing development time of electric machines with SyMSpace," in *Proc. 8th Int. Electric Drives Prod. Conf. (EDPC)*, Dec. 2018, pp. 1–5.
[34] A.-C. Zăvoianu, G. Bramerdorfer, E. Lughofer, W. Amrhein, and E. P. Klement, "DECMO2: A robust hybrid and adaptive multi-objective evolutionary algorithm," *Soft Comput.*, vol. 19, no. 12, pp. 3551–3569, 2014.
[35] *DR.71.J–DR.100.J AC Motors with LSPM Technology*. SEW-EURODRIVE. Accessed: Apr. 10, 2021. [Online]. Available: https://download.sew-eurodrive.com/download/pdf/21281793.pdf

JAN BARTA was born in Novy Jicin, Czech Republic, in 1989. He received the B.Sc., M.Sc., and Ph.D. degrees in power electrical and electronic engineering from Brno University of Technology, Brno, Czech Republic, in 2012, 2014, and 2018, respectively.

From 2014 to 2018, he was a Member of Technical Staff at Brno University of Technology, where he was conducting research on electrical machines. He is currently an Assistant Professor with the Department of Power Electrical and Electronic Engineering, Brno University of Technology. His research interests include line-start synchronous machines, and high-speed and high-efficiency electrical machines.

LADISLAV KNEBL was born in Lichnov, Czech Republic, in 1993. He received the B.Sc. and M.Sc. degrees in power electrical and electronic engineering from Brno University of Technology, Brno, Czech Republic, in 2015 and 2017, respectively, where he is currently pursuing the Ph.D. degree with the Department of Power Electrical and Electronic Engineering.

He worked with the Department of Research and Development, Baumüller Brno Ltd., from 2015 to 2017. He was engaged in assisted synchronous reluctance machines development and the designing of tools focused on interior permanent magnet motors. His research interests include open-source FEA programs and the development of assisted synchronous reluctance motors.

GERD BRAMERDORFER (Senior Member, IEEE) received the Ph.D. degree in electrical engineering from Johannes Kepler University Linz, Austria, in 2014.

He is currently an Assistant Professor with the Department of Electrical Drives and Power Electrionics, Johannes Kepler University Linz. His research interests include the design, modeling, and optimization of electric machines as well as magnetic bearings and bearingless machines. He is an Editor of the IEEE TRANSACTIONS ON ENERGY CONVERSION and a past Associate Editor of the IEEE TRANSACTIONS ON INDUSTRIAL ELECTRONICS.

IVETA LOLOVA received the B.Sc. and M.Sc. degrees in power electrical and electronic engineering from Brno University of Technology, Brno, Czech Republic, in 2018 and 2020, respectively, where she is currently pursuing the Ph.D. degree with the Department of Power Electrical and Electronic Engineering.

Since 2018, she has been a Member of Technical Staff at Brno University of Technology, where she is conducting research on electrical machines. Her research interests include line-start electrical machines and topology optimization of electrical machines.

Ms. Lolova is a holder of Brno Ph.D. Talent Scholarship funded by Brno City Municipality.

SIEGFRIED SILBER (Member, IEEE) received the Dipl.-Ing. degree in electrical engineering from Graz University of Technology, in 1995, and the Dr.techn. degree from Johannes Kepler University Linz, Linz, Austria, in 2000.

He was with the Institute for Electrical Drives and Power Electronics, Johannes Kepler University Linz, from 1995 to 2014, and joined Linz Center of Mechatronics (LCM), in 2014, where he is currently the Team Leader in the area electrical drives. He is leading the development of a software tool for the optimization of electrical drives (SyMSpace). His research interests include electrical drives, power electronics, and magnetic bearings and bearingless motors.

ONDREJ VITEK was born in Vsetin, Czech Republic, in 1979. He received the M.Sc. and Ph.D. degrees in electrical engineering from Brno University of Technology, Czech Republic, in 2003 and 2006, respectively.

Since 2006, he has been working with Brno University of Technology, where he is currently an Associate Professor and the Head of the Department of Power Electrical and Electronic Engineering. His main research interest includes design, modeling, and diagnosis of electrical machines.